Journal of Nuclear Materials 429 (2012) 245–256

Contents lists available at SciVerse ScienceDirect

Journal of Nuclear Materials

journal homepage: www.elsevier.com/locate/jnucmat

Mathematical modeling of cold cap

Richard Pokorny [a], Pavel Hrma [b,c,*]

[a] Department of Chemical Engineering, Institute of Chemical Technology in Prague, Technicka 5, 166 28 Prague 6, Czech Republic
[b] Pacific Northwest National Laboratory, Richland, WA 99352, USA
[c] Division of Advanced Nuclear Engineering, Pohang University of Science and Technology, Pohang, Republic of Korea

ARTICLE INFO

Article history:
Received 3 October 2011
Accepted 6 June 2012
Available online 16 June 2012

ABSTRACT

The ultimate goal of studies of cold cap behavior in glass melters is to increase the rate of glass processing in an energy-efficient manner. Regrettably, mathematical models, which are ideal tools for assessing the responses of melters to process parameters, have not paid adequate attention to the cold cap. In this study, we consider a cold cap resting on a pool of molten glass from which it receives a steady heat flux while temperature, velocity, and extent of conversion are functions of the position along the vertical coordinate. A one-dimensional mathematical model simulates this process by solving the differential equations for mass and energy balances with appropriate boundary conditions and constitutive relationships for material properties. The sensitivity analyses on the effects of incoming heat fluxes to the cold cap through its lower and upper boundaries show that the cold cap thickness increases as the heat flux from above increases, and decreases as the total heat flux increases. We also discuss the effects of foam, originating from batch reactions and from redox reactions in molten glass, and argue that models must represent the foam layer to achieve a reliable prediction of the melting rate as a function of feed properties and melter conditions.

1. Introduction

Glass batch melting has been investigated, both experimentally and by mathematical modeling, to gain deeper understanding of the process and to assist in furnace development [1]. Most modeling literature pertains to melting in fuel-fired furnaces; somewhat less to melting in all-electric melters. However, mathematical models of glass-melting furnaces, even those most recent [2–5], rarely model the batch conversion process. Instead, they assume a uniform inlet velocity with a prescribed temperature at the batch-melt interface without considering gas bubbles under the batch pile (although Moukarzel and Kuhn [2] mentioned the Rayleigh–Bénard instability caused by the density gradient). Only a handful of researchers (Mase and Oda [6], Viskanta and Wu [7], Ungan and Viskanta [8], Hrma [9], Schill [10,11], and Pokorny et al. [12,13] developed simplified one-dimensional (1D) or two-dimensional (2D) models for the batch piles charged into gas-heated furnaces.

The proclaimed goals of mathematical models of glass-melting furnaces are identifying probable sources of flaws and improving melter design and operation with respect to glass quality and the rate of production. For the vitrification of radioactive wastes, which is performed almost exclusively in Joule-heated or induction-heated electrical furnaces, the rate of melting is the primary concern because it directly influences the life cycle of nuclear waste cleanup. Mathematical modeling can hardly achieve these objectives without an adequate model for the batch. As Schill pointed out [14], the batch melting process influences the velocity and temperature fields inside the entire furnace. This is particularly true for the all-electric furnaces, where the cold cap covers most of the melt surface area.

All-electric melters provide us with the simplest case for a mathematical model of batch melting. An assumption that the particles of batch, or melter feed, move vertically down through the cold cap greatly simplifies mathematical treatment: at a sufficient distance from the edges, the melting process can be treated as 1D. Because batch reactions are complex and numerous, further simplifications are needed. Processes such as water evaporation, gas evolution, melting of salts, borate melt formation, reactions of borate melt with molten salts and amorphous solids, precipitation of intermediate crystalline phases, formation of a continuous glass-forming melt, growth and collapse of primary foam, and dissolution of residual solids must be accounted for. To this list, we also need to add the formation of secondary foam originating from molten glass, but accumulating at the bottom of the cold cap. This complex situation is simplified by treating the reacting mixture as consisting of just two phases, the condensed phase (all solids and liquids) and the gas phase.

This paper presents a 1D model of a cold cap in a melter for high-level-waste vitrification. The melter is charged with melter feed in the form of slurry containing 40–60% water. The particular

* Corresponding author at: Division of Advanced Nuclear Engineering, Pohang University of Science and Technology, Pohang, Republic of Korea.
E-mail address: pavelhrma@postech.ac.kr (P. Hrma).

0022-3115/$ - see front matter © 2012 Elsevier B.V. All rights reserved.
http://dx.doi.org/10.1016/j.jnucmat.2012.06.013

Nomenclature

A	area (m^2)
a	thermal diffusivity ($m^2\ s^{-1}$)
c	heat capacity ($J\ kg^{-1}\ K^{-1}$)
g	gravitational constant ($m\ s^{-2}$)
h	heat transfer coefficient ($W\ m^{-2}\ K^{-1}$)
h	thickness (m)
H	heat source ($W\ m^{-2}$)
ΔH	specific heat ($J\ kg^{-1}$)
j	mass flux ($kg\ m^{-2}\ s^{-1}$)
k	conversion rate coefficient (s^{-1})
L	characteristic length (m)
m	mass (kg)
N	number of nodal points (–)
Nu	Nusselt number (–)
p	void fraction/porosity (–)
q	heat flux ($W\ m^{-2}$)
Q	heat flux ($W\ m^{-2}$)
r	mass change rate ($kg\ m^{-3}\ s^{-1}$)
R	radius (m)
Ra	Rayleigh number (–)
s	internal heat source ($W\ m^{-3}$)
t	time (s)
T	temperature (K)
v	velocity ($m\ s^{-1}$)
V	volume (m^3)
x	global coordinate (m)

Greek letters

β	thermal expansion coefficient (K^{-1})
δ	space step (m)
δ	layer thickness (m)
ε	absolute tolerance (K)
ε	emissivity (–)
θ	contact angle (rad)
λ	heat conductivity ($W\ K^{-1}\ m^{-1}$)
μ	dynamic viscosity (Pa s)
ν	kinematic viscosity ($m^2\ s^{-1}$)
ξ	degree of conversion (–)
ρ	density ($kg\ m^{-3}$)
σ	surface tension ($kg\ s^{-2}$)
τ	time step (s)
Φ	heating rate ($K\ min^{-1}$)

Sub- and superscripts

b	bulk/condensed phase
B	bottom
C	critical
C	conversion controlled
c	condensed
cav	cavity
cond	conductive
conv	convective
D	dry batch
E	evaporation
Eff	effective
f	foam
F	feed
g	gas phase
H	heat transfer controlled
i	space node index
k	time node index
M	melt
p	capillary
P	preheating
P	primary foam
rad	radiation
S	slurry
S	secondary foam
T	top
U	upper
V	vapor
W	water

melter feed chosen for this study has been formulated to vitrify one of the nuclear wastes considered for the Waste Treatment and Immobilization Plant, currently under construction at the Hanford Site in Washington State, USA. However, the paper is more focused on the model development than on a particular waste stream, which was selected solely because it has been reasonably well, though not yet completely, characterized regarding the key properties and the reaction kinetics [15–19]. The model itself is based on the ideas elaborated by Hrma [9] and Schill [10,11], and represents a step toward the formulation of a 3D version that can be incorporated in the mathematical models of the whole melter. The final outcome of the combined 3D model will be a reliable prediction of the melting rate by means of computation, thus assisting expensive and time-consuming empirical development of melter design and operation.

2. Theory

Glass batch, or melter feed, is a heterogeneous mixture of multiple solids. In an electrical melter, the batch in the form of slurry feed is charged from the top, creating a cold cap on the pool of molten glass. The 1D model views the cold cap as a blanket of uniform thickness that receives steady uniform heat fluxes from both the molten glass below and the plenum space above.

Under optimal steady-state conditions, each particle of the melter feed travels vertically down through the cold cap, experiencing increasing temperature in response to which its properties (e.g., density, dissolution rates of solids, reaction kinetics) are changing. Thus, as the feed-to-glass conversion progresses, the temperatures, velocities, and extents of feed reactions are

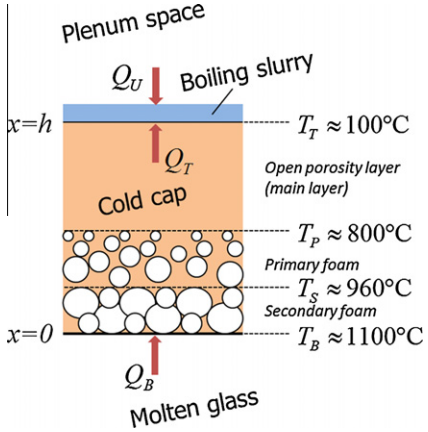

Fig. 1. Cold cap structure.

functions of a single variable, the position along the vertical coordinate, x, with the origin located at the cold cap bottom (Fig. 1).

During the melting, multiple overlapping reactions occur, producing gases (H_2O, CO_x, NO_x, and O_2), liquids (molten salts and glass-forming melts), and intermediate solids. Within the cold cap, the individual phases move with different velocities. For simplicity, as discussed, we consider a two-phase model in which the melter feed is a mixture of the condensed phase, comprising liquids and solids, and the gas phase. Each phase exchanges mass and energy with the other phase.

2.1. Mass balance

Neglecting diffusion, the mass balances of the condensed phase and the gas phase are:

$$\frac{d\rho_b}{dt} + \frac{d(\rho_b v_b)}{dx} = r_b \tag{1}$$

$$\frac{d\rho_g}{dt} + \frac{d(\rho_g v_g)}{dx} = r_g \tag{2}$$

where t is the time, ρ the spatial density, v the velocity, r the mass source associated with reactions, and the subscripts b and g denote the condensed phase and the gas phase, respectively. The time derivatives are zero in the steady state. By the mass conservation law, $r_b + r_g = 0$. The mass fluxes, j_b and j_g are defined as:

$$j_b = -\rho_b v_b \tag{3}$$

$$j_g = \rho_g v_g \tag{4}$$

Because the condensed phase moves in the negative direction, the minus sign is used in Eq. (3) to obtain a positive flux. With these definitions, at a steady state, the sources and fluxes are related as:

$$j_g(x) = \int_0^x r_g dx \tag{5}$$

$$j_{gT} = \int_0^h r_g dx \tag{6}$$

where h is the cold cap thickness, and j_{gT} is the gas flux leaving the cold cap through the top.

The degree of conversion with respect to the gas production is defined as:

$$\xi_g(x) = 1 - j_g(x)/j_{gT} \tag{7}$$

According to the mass conservation law, the difference between the mass flux of the condensed phase to and from the cold cap is:

$$\Delta j_b = j_T - j_M = j_{gT} \tag{8}$$

where j_T is the mass flux of the condensed phase (dry melter feed) entering the cold cap on the top, and j_M is the mass flux of the condensed phase (molten glass) leaving the cold cap from the bottom. Using Eqs. (7) and (8), the mass flux of the gas phase can also be expressed using the degree of conversion and the mass loss of the condensed phase:

$$j_g(x) = \Delta j_b(1 - \xi_g(x)) \tag{9}$$

satisfying the condition $j_g(h) = \Delta j_b$. According to Eqs. (7)–(9), the mass flux of the condensed phase at any position is related to the degree of conversion with respect to gas:

$$j_b(x) = j_T - \Delta j_b \xi_g(x) \tag{10}$$

2.2. Energy balance

Chemical reactions and physical–chemical processes that occur while the melter feed undergoes melting absorb or evolve heat in addition to the sensible heat. The energy balance was used in the form:

$$\rho_b c_b \frac{dT_b}{dt} = -\rho_b v_b c_b \frac{dT_b}{dx} - \frac{dq_b}{dx} + H + s \tag{11}$$

$$\rho_g c_g \frac{dT_g}{dt} = -\rho_g v_g c_g \frac{dT_g}{dx} - \frac{dq_g}{dx} - s \tag{12}$$

where T is the temperature, c is the heat capacity, q is the heat flux, H is the internal heat source, and s is the heat transfer between phases. Summing Eqs. (11) and (12), using Eqs. (3) and (4), neglecting the heat accumulation term in gas ($\rho_g c_g \ll \rho_b c_b$), and assuming instantaneous heat equilibrium between the gas and the condensed phase ($T_g = T_b = T$), the energy balance becomes:

$$\rho_b c_b \frac{dT}{dt} = (j_b c_b - j_g c_g)\frac{dT}{dx} - \frac{dq}{dx} + H \tag{13}$$

where $q = q_b + q_g$.

The values of material parameters, such as the heat conductivity, heat capacity, reaction heat, and density, vary with temperature and composition. The change in temperature is also accompanied by the change in texture (e.g., the interface area between phases).

The heat fluxes are subjected to Fourier's law, where the effective value of heat conductivity, λ^{Eff}, is assumed to involve both conductive and radiative modes of heat transfer in the feed:

$$q = -\lambda^{Eff}\frac{dT}{dx} \tag{14}$$

Because the heat conductivity of gas is low [$\lambda_g(CO_2, 200\,^\circ C) = 0.03\ W\ m^{-1}\ K^{-1}$], $\lambda^{Eff} = \lambda_b$ everywhere except in foam.

Since the condensed phase and gas phase have a common temperature, Eqs. (11) and (13) yield:

$$s = -\rho_g v_g c_g \frac{dT}{dx} = -j_g c_g \frac{dT}{dx} \tag{15}$$

The boundary conditions can be given in terms of fluxes, temperatures, or both:

$$q_b(0) = Q_B \tag{16}$$

$$q_b(h) = Q_T \tag{17}$$

$$T(0) = T_B \tag{18}$$

$$T(h) = T_T \tag{19}$$

where T_B and T_T are the bottom and top cold cap temperatures, respectively, and Q_B and Q_T are the heat fluxes to cold cap bottom and from cold cap top, respectively.

2.3. Schemes for numerical calculations

To solve the energy balance equation, we used, for the sake of simplicity and comprehensibility, the finite difference method. In terms of explicit finite differences, Eq. (13) becomes (Schill [11]):

$$\rho_{bi}^k c_{bi}^k \frac{T_i^{k+1} - T_i^k}{\tau} = (j_{bi}^k c_{bi}^k - j_{gi}^k c_{gi}^k)\frac{T_{i+1}^k - T_{i-1}^k}{2\delta} + \lambda_{i+}^k \frac{T_{i+1}^k - T_i^k}{\delta^2} - \lambda_{i-}^k \frac{T_i^k - T_{i-1}^k}{\delta^2} + H_i^k$$
$$i = 2, \ldots, N-1 \tag{20}$$

where δ is the space step (nodal points are represented by the subscript i), τ is the time step (represented by the superscript k) and N is the number of nodal points. Here, λ^k_{i+} and λ^k_{i-} are the mean values of heat conductivity between adjacent nodal points:

$$\lambda^k_{i+} = \frac{\lambda^k_i + \lambda^k_{i+1}}{2} \tag{21}$$

$$\lambda^k_{i-} = \frac{\lambda^k_i + \lambda^k_{i-1}}{2} \tag{22}$$

and represent effective values of heat conductivity of the cold cap. For a reasonably fast convergence and sufficient accuracy, the usual values of space and time steps were 1 mm and 0.1 s respectively (typical values of the cold cap thickness and the time to reach the steady state are 60 mm and 5×10^4 s). Further decrease in the space and time steps is not useful because it leads to slower convergence, and the accuracy is already at an acceptable level for our purpose.

The set of equations in Eq. (20) needs to be supplied with boundary conditions. Dirichlet conditions directly represent the values of boundary temperatures; according to Eqs. (18) and (19), $T^k_1 = T_B$ and $T^k_N = T_T$ for every time step k. On the other hand, Neumann boundary conditions specify the heat flux. Together with the Dirichlet condition, Eq. (16), (17), the combined boundary conditions combine T^k_N and:

$$q_1 = \lambda^k_1 \frac{T^k_2 - T^k_1}{\delta} + \frac{\delta \rho^k_{b1} c^k_{b1}}{\tau}(T^{k+1}_1 - T^k_1) \tag{23}$$

where $q_1 = Q_B$ is the heat flux from the melt to the cold cap.

For numerical simulations, experimental data were used together with constitutive equations that were taken from the literature and modified for our problem as described in Section 3. The mass flow of the condensed and gas phases was calculated from thermogravimetric analysis (TGA) data. Because the results from differential scanning calorimetry (DSC) experiments provide us with the effective value of heat capacity including the reaction heat, we also needed to modify the energy balance accordingly:

$$\rho^k_{bi} c^k_{bi} \frac{T^{k+1}_i - T^k_i}{\tau} = (j^k_{bi} c^{k,Eff}_{bi} - j^k_{gi} c^k_{gi}) \frac{T^k_{i+1} - T^k_{i-1}}{2\delta} + \lambda^k_{i+} \frac{T^k_{i+1} - T^k_i}{\delta^2} - \lambda^k_{i-} \frac{T^k_i - T^k_{i-1}}{\delta^2} \tag{24}$$

where $c^{k,Eff}_{bi}$ represents the effective value of heat capacity with the reaction heat:

$$j^k_{bi} c^{k,Eff}_{bi} \frac{T^k_{i+1} - T^k_{i-1}}{2\delta} = (j^k_{bi} c^k_{bi}) \frac{T^k_{i+1} - T^k_{i-1}}{2\delta} + H^k_i \tag{25}$$

Eq. (24) was iteratively solved together with chosen boundary conditions. The simulation was stopped when the temperature field was no longer changing with time, satisfying the condition:

$$|(T^{k+1}_i - T^k_i)| \leqslant \varepsilon (i = 1, 2, \ldots, N) \tag{26}$$

where ε is the absolute tolerance (usually $\varepsilon = 10^{-5}$ K). The resulting temperature field was then considered a stationary solution of Eq. (13). All algorithms were coded in Mathworks MATLAB 7.

3. Material properties

To solve the heat and mass balance equations, we need to express the material properties as functions of temperature and composition. To this end, we selected a melter feed of the composition shown in Table 1, which was designed to vitrify high-alumina high-level waste and has previously been characterized in several experimental studies [15–19].

Table 1
Melter feed composition (in g) to make 1 kg of glass.

Compound	g/kg
$Al(OH)_3$	367.49
SiO_2	305.05
$B(OH)_3$	269.83
NaOH	97.14
Li_2CO_3	88.30
$Fe(OH)_3$	73.82
CaO	60.79
NaF	14.78
$Bi(OH)_3$	12.80
$Fe(H_2PO_2)_3$	12.42
Na_2CrO_4	11.13
$NiCO_3$	6.36
$Pb(NO_3)_2$	6.08
$Zr(OH)_4{\cdot}0.654H_2O$	5.11
$NaNO_3$	4.93
Na_2SO_4	3.55
$NaNO_2$	3.37
KNO_3	3.04
$Zn(NO_3)_2{\cdot}4H_2O$	2.67
$Na_2C_2O_4{\cdot}3H_2O$	1.76
$Mg(OH)_2$	1.69
Totals	1352.11

3.1. Degree of conversion and heat capacity

Fig. 2 shows the mass loss fraction and the corresponding rate of gas-phase production together with the degree of conversion (inset), calculated as:

$$\xi_g(T) = \frac{m(T) - m_F}{m_M - m_F} \tag{27}$$

where $m(T)$ is the temperature-dependent sample mass, m_F is the melter-feed mass, and m_M is the glass mass. This definition is equivalent to Eq. (7). In terms of TGA data, m_F is the initial sample mass, and m_M is the sample mass after major gas evolution stopped (above ~630 °C) but before the glass mass began to decrease because of volatilization (above ~1000 °C). The dry melter feed of composition shown in Table 1 evolves 1.32×10^3 m^3 of gas per kg of glass at 630 °C (1.20×10^3 m^3 H_2O, 94 m^3 CO_2, 14 m^3 NO, and 9 m^3 O_2). Though most of this gas evolves below 630 °C, a smaller fraction, undetectable by TGA, continues evolving as temperature increases with significant consequences for the rate of melting (see Sections 3.2 and 4.4).

The "effective" heat capacity of the melter feed, c^{Eff}_b, was measured with the DSC as displayed in Fig. 3. The dashed line represents the estimated true heat capacity. Because the instrument did not yield reliable data at $T > 850$ °C, and because major batch reactions are complete by 800 °C, we assumed that the heat capacity was constant at $T \geqslant 850$ °C. The peaks are associated with the endothermic reactions, such as releasing of bonded water.

Following Schill [11], the heat capacity of the gas phase was approximated by that of carbon dioxide:

$$c_g(T) = 1003 + 0.21T - \frac{1.93 \cdot 10^7}{T^2} \quad (c_g \text{ in J kg}^{-1}\text{ K}^{-1} \text{ and } T \text{ in K}, T \geqslant 373 \text{ K}) \tag{28}$$

3.2. Density

The melter feed density was estimated from pellet expansion data (displayed in Fig. 4) and from the loose-batch data reported in [15]. The volume of both loose batch and pellets changed little initially while batch gases evolved. Gases were escaping through

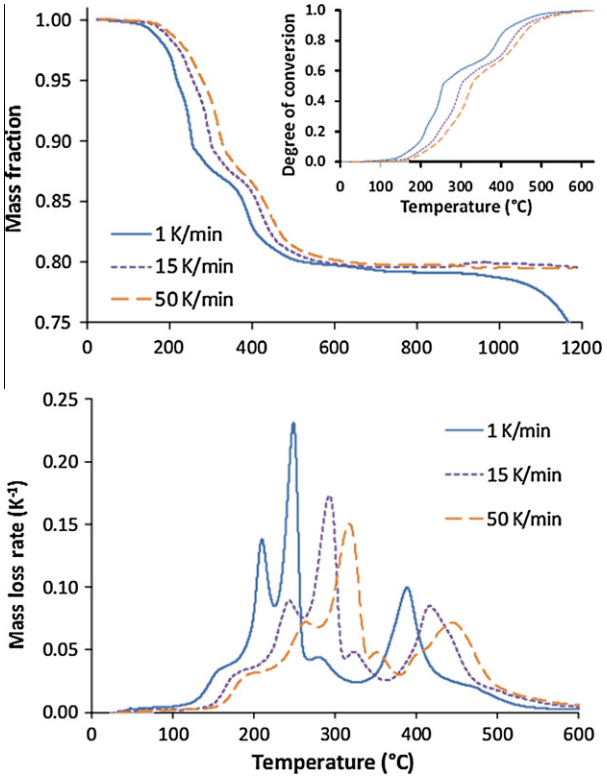

Fig. 2. Melter-feed mass loss, degree of conversion with respect to gas phase (inset), and mass loss rate versus temperature and heating rate.

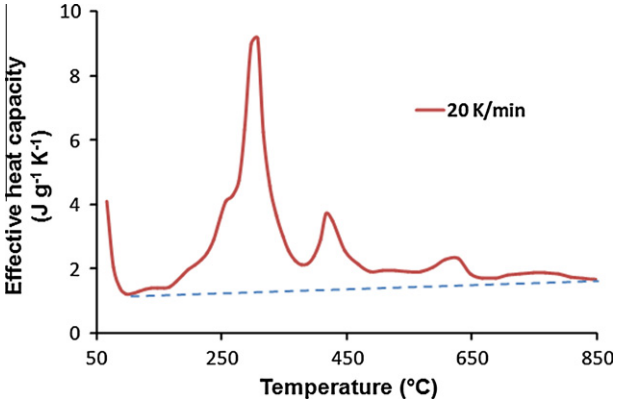

Fig. 3. Melter-feed effective heat capacity (solid line) and estimated true heat capacity (dashed line) versus temperature for 20 K min^{-1} heating rate.

open pores even while melter feed was shrinking, starting at ~700 °C to a minimum volume at ~800 °C. Above ~800 °C, the glass-forming melt became connected and open pores turned into bubbles while gases continued to evolve. As temperature increased, the melt expanded to foam that eventually collapsed at ~900–1000 °C, most likely by internal coalescence of bubbles into large cavities as a result of pressure from evolving gases and rapidly decreasing melt viscosity.

As described by Henager et al. [16], the normalized area, shown in Fig. 4, was transformed to the volume, thus allowing the calculation of the void fraction and the density. The initial density of loose melter feed was ρ_{b0} = 970 kg m^{-3} [15]. The density decreased as the temperature increased as a result of mass loss and the nearly constant volume of the sample at T < ~700 °C, i.e., $\rho_b(T) = \rho_{b0} m(T)/$

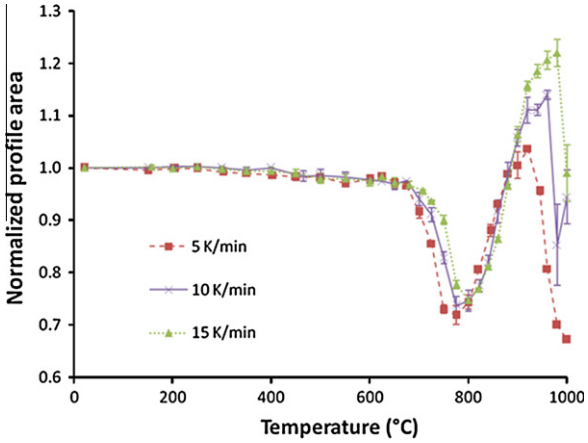

Fig. 4. Normalized melter-feed-pellet profile area versus temperature and heating rate.

m_F. Once the sample was shrinking between ~700–800 °C, the density increased to a maximum. It can be assumed that the bulk density and porosity were not affected by the initial compression of pellets at and above the minimum-volume temperature of ~800 °C. Then, above 800 °C, the density decreased as the bubbly melt turned to foam, reaching a minimum. For a heating rate of 15 K min^{-1}, the minimum density of 541 kg m^{-3} was reached at ~960 °C when the void fraction increased to an unsustainable value of 0.79.

In a melter feed sample, loose batch or pellet, foam collapses between ~960 and 1100 °C. However, as argued in Sections 4 and 5, the density of the secondary foam layer (see Fig. 1), occurring within the temperature interval from ~960 to 1100 °C, remains constant.

3.3. Heat conductivity

Fig. 5 shows apparent effective heat conductivities of glass batches compiled from the literature including data reported by Hrma et al. [15] for a melter feed of a composition similar to that used in this work. Data by Lottes and Petrick [20], Viskanta and Wu [7], and Schill [11] pertain to commercial batches. The effective heat conductivity involves both conduction and radiation heat transfer. The apparent effective conductivity shown in Fig. 5 is influenced by the enthalpies of reactions occurring during melting.

Additional data were reported by Faber et al. [21], Conradt et al. [22], and Kham [23]. Faber et al. [21] measured the effective thermal diffusivity (a) of batches as a function of temperature, obtaining a typical value of 4×10^{-7} m^2 s^{-1} at temperatures <900 °C; at temperatures >900 °C, the value increased, reaching 4×10^{-6} m^2 s^{-1} at

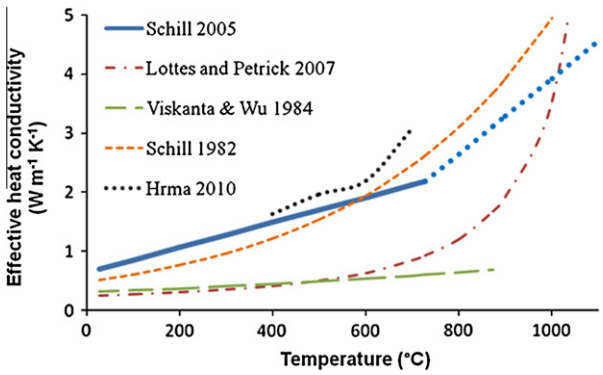

Fig. 5. Melter-feed effective heat conductivity versus temperature.

1100 °C. Conradt et al. [22] obtained $a \sim 1 \times 10^{-7}$ m^2 s^{-1} at <900 °C and $\sim 4 \times 10^{-7}$ m^2 s^{-1} at >900 °C. When foam developed within the batch, a did not increase until the temperature approached 1100 °C. Kham [23] measured a for various commercial batches; a gradually increased from $\sim 3.5 \times 10^{-7}$ m^2 s^{-1} at 350 °C to $\sim 4 \times 10^{-7}$ m^2 s^{-1} at 650 °C. Values recently obtained for high-level waste batches [15] for <700 °C were of the order 10^{-6} m^2 s^{-1}.

For our modeling, we selected data reported by Schill [24] for a high-level waste melter feed:

$$\lambda^{Eff} = 0.06571 + 0.002114T \quad (\lambda \text{ in W m}^{-1}\text{ K}^{-1} \text{ and } T \text{ in K, } 373\text{ K} < T < 1000\text{ K}) \tag{29}$$

We used a linear interpolation between 1000 K and the heat conductivity value of molten glass at 1373 K (1100 °C), λ^{Eff}(1100 °C) = 4.56 W m^{-1} K^{-1} (Schill [24]), as is indicated in Fig. 5:

$$\lambda^{Eff} = -4.2007 + 0.0063807T \quad (\lambda \text{ in W m}^{-1}\text{ K}^{-1} \text{ and } T \text{ in K, } 1000\text{ K} < T < 1373\text{ K}) \tag{30}$$

Complications arise when considering the foam layer—see Sections 4 and 5.

4. Cold cap thickness

Fig. 1 illustrates the simplified 1D representation of the cold cap. A layer of boiling slurry rests on the top of the cold cap, which consists of two layers: the main layer in which batch reactions occur and batch gases are escaping through open pores, and the bottom foam layer.

Foam at the bottom of the cold cap arises in two ways. Primary foam is formed by batch gases trapped in the glass-forming melt. Secondary foam results from the accumulation of bubbles from redox reactions. It is highly plausible that the foam layer has a low-heat conductivity; thus, the foam layer hinders the heat transfer to the cold cap and leads to a lower melting rate [17]. To the best of our knowledge, the heat conductivity of the foam layer has not been determined experimentally. The foam layer issues, including heat conductivity, are addressed in Section 5. In Section 5.5, the heat conductivity of the foam layer is estimated to be close to half of the heat conductivity of bubble-free melt. Thus, for the purpose of modeling, we assumed that the heat conductivity of the foam layer within the cold cap equals half of the heat conductivity of the bubble-free cold cap.

4.1. Boundary conditions and the baseline case

The boundary temperatures and heat fluxes are illustrated in Fig. 1. For the calculations, the cold cap bottom temperature was T_B = 1100 °C (the estimated temperature of molten glass under the foam layer), and the temperature at the interface between the cold cap and the slurry layer was T_T = 100 °C (the temperature of the boiling slurry pool, ignoring the boiling point elevation by dissolved salts). The foam layer upper temperature was T_P = 800 °C (the minimum on the feed expansion curve, see Fig. 4).

As a baseline case, we chose a slurry feed containing 52.2 mass% of water and the glass production rate (the rate of melting) 1220 kg m^{-2} day^{-1} (j_M = 0.0141 kg m^{-2} s^{-1}), a realistic situation considering melter experiments reported by Matlack et al. [25]. The corresponding rates of slurry-feed charging and dry-melter-feed charging are j_S = 0.037 kg m^{-2} s^{-1} and j_T = 0.0177 kg m^{-2} s^{-1} (to simplify the notation, subscript b is dropped from j_b).

The mass flux of water, j_W, is 0.0193 kg m^{-2} s^{-1}. With the evaporation heat of water ΔH_W = 2.26 MJ kg^{-1}, the heat flux to evaporate water is $Q_E = j_W\,\Delta H_W$ = 43.6 kW m^{-2}. The heat to preheat the slurry to the temperature of the boiling slurry (~100 °C) is $Q_P = (j_W c_{p,W} + j_D c_{p,D})(T_2 - T_1)$ = 7.3 kW m^{-2}, where j_D is the mass flux of dry batch and $c_{p,D}$ is its heat capacity. Thus, the heat flux to turn the slurry into dry feed is $Q_S = Q_P + Q_E$ = 50.9 kW m^{-2}. This heat flux is coming from both the molten glass and plenum space. Finally, the heat flux to melt the 100 °C dry melter feed to 1100 °C molten glass, calculated from DSC data (Fig. 3), is Q_D = 33.8 kW m^{-2}. The total heat flux to convert the slurry to 1100 °C melt is $Q_F = Q_S + Q_D$ = 84.7 kW m^{-2}.

Because the cold cap does not cover the entire melt surface area (typically, 90–95% coverage), the heat flows from the free surface of molten glass to the plenum space by radiation as well as conduction/convection. A part of this heat flux is lost to the ambient and the rest helps to preheat the slurry, evaporate water, and heat the steam. Thus, the major part of the total heat flux to convert the slurry to molten glass at 1100 °C comes from the cold cap bottom (Q_B), of which a part enters the boiling slurry (Q_T), while the remaining heat flows to boiling slurry from the plenum space (Q_U). In Section 4.5, the sensitivity analysis explores the effects of the boundary heat fluxes, Q_B and Q_U, on the cold cap thickness.

The heat flux to heat the vapor from 100 °C to 350 °C is $Q_V = j_V c_{p,V}\ (T_2 - T_1)$ = 9.7 kW m^{-2}. However, the plenum space, where the steam is heated from ~100 °C to 350–450 °C, is not included in the 1D cold cap model.

4.2. Reaction kinetics

Because the reaction kinetic data were not yet available in a form suitable for mathematical modeling while performing the calculations, we used the degree of conversion based on experimental data for the heating rate $\Phi = dT/dt$ = 15 K min^{-1} (TGA) instead of employing reaction kinetics in the form of differential equations. This simplification is unlikely to significantly affect the results of computation because, as can be seen in the top diagram in Fig. 2, the $\xi_g(T)$ function changes little with the rate of heating. Above 800 °C, the batch reactions are completed and only oxygen-evolving redox reactions occur, but the effect of redox reactions on melter-feed mass and energy is miniscule and can be neglected (though their effect on foaming and heat transfer is substantial).

4.3. Effect of heat fluxes on temperature profile

Table 2 and Fig. 6 compare the results for three values of the fractional heat flux from above, Q_U/Q_S, while the total heat flux supplied to the slurry layer is constant. The temperature profiles exhibit three intervals with distinct temperature gradients. Starting from the cold cap bottom, the interval from 1100 °C to 800 °C pertains to the foam layer with a steep temperature gradient caused by the low effective heat conductivity. Above the foam layer, the temperature gradient decreases again between 250 and 350 °C because of the endothermic melting reactions. As Fig. 6 shows, Q_U/Q_S strongly affects the temperature field, and thus the cold cap thickness.

4.4. Profiles of velocity and key properties

Figs. 7–9 display profiles of condensed phase velocity and key properties within the cold cap for Q_U/Q_S = 0.8. Fig. 7 shows the bulk density and velocity versus x. In the upper part of the cold cap, the density decreases with decreasing x as a result of gas-evolving reactions until it begins to sharply increase within the short interval of melter-feed shrinking. Above 800 °C, the abrupt decrease of density occurs in the foam layer.

The high porosity of the foam layer results in a higher velocity of the condensed phase. The lowest velocity within the cold cap occurs just above the foam layer where the porosity reaches

Table 2
Cold cap thickness, time in the cold cap, average rate of heating, and heat fluxes to cold cap and boiling slurry as functions of Q_U/Q_S.

Q_U/Q_S	h (mm)	Δt (min)	Φ (K min^{-1})	Q_U (kW m^{-2})	Q_T (kW m^{-2})	Q_B (kW m^{-2})	Q_F (kW m^{-2})
0.0	2.3	22.2	45.0	0	50.9	84.7	84.7
0.5	3.7	35.4	28.3	25.4	25.5	59.3	84.7
0.8	6.0	56.5	17.7	40.7	10.2	44.0	84.7

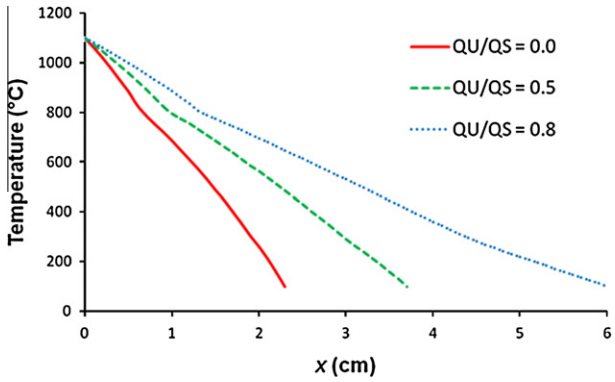

Fig. 6. Cold cap temperature profile for three heat fluxes from plenum space.

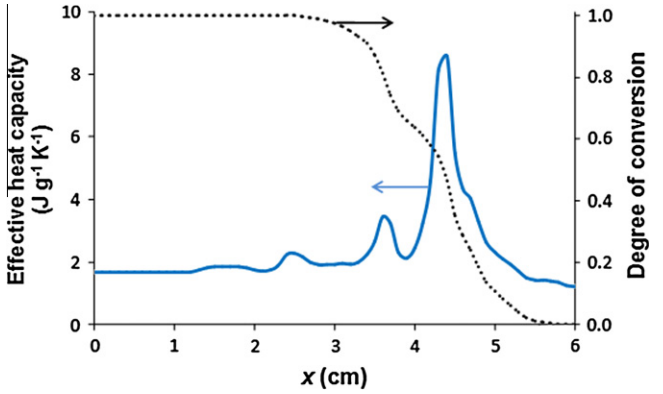

Fig. 8. Degree of conversion with respect to gas phase and effective heat capacity distributions within cold cap.

minimum. In the upper part of the cold cap, velocity is close to constant. Based on the experimental data of melter-feed-volume expansion in response to heating, the mass flux can be expressed as $j(T) = j_T m(T)/m_F$. By Eq. (3), $j(T) = -v(T)\rho(T)$. Accordingly, $j(T) = -v(T)m(T)/V(T)$, where $V(T) = m(T)/\rho(T)$ is temperature-dependent volume of the feed sample. Thus, the condensed phase velocity can be expressed as $v(T) = -j_T V(T)/m_F$. According to this equation, v is directly proportional to the sample volume measured in expansion experiments and is constant when V is constant.

Fig. 8 shows that gas-evolving reactions take place, and that most of the heat for melting is consumed, in the upper part of the cold cap (0.5–4 cm below the top surface). This heat and the heat to evaporate water needs to be transferred through the foam layer. Note that a small amount of gas evolved in the lower part of the cold cap is responsible for primary foaming. Gas evolution above 650 °C was not detected as a mass loss by TGA, but was clearly detected by the gas-chromatography/mass-spectrometry instrument for similar melter feeds [26,27].

Fig. 9 shows the abrupt drop in the heat conductivity caused by the presence of the foam layer. Above the foam layer, the heat conductivity follows the trend determined by Eqs. (29) and (30) as shown in Fig. 5. Within the foam layer, it drops and increases towards the cold cap bottom, where it jumps back to that of molten glass. This is what one would expect to occur in an opaque melt. Even in transparent glass, the presence of foam prevents the dramatic increase of the heat conductivity by radiative transfer [22].

4.5. Effect of heat fluxes on cold cap thickness

Fig. 10 displays the thickness of the cold cap as a function of Q_U/Q_S for different values of Q_F, i.e., different rates of melting. An increased heat flux from the plenum results in a thicker cold cap. Consequently, the feed experiences a lower heating rate (see Table 2), thus allowing more time for batch reactions to progress at lower temperatures. As discussed in Section 5.3, a lower heating rate results in lower foaming. This in turn allows the heat transfer from melt to the cold cap to increase, and consequently increase the rate of melting. As Fig. 10 shows, a higher melting rate makes the cold cap thinner. One can expect that a thickness exists that balances, via foaming, the heat fluxes from the top and bottom of the cold cap.

One can suspect that a substantial increase in the cold cap thickness may lead to the "frozen cold cap" when the fluxes (molten salt of a low viscosity) are drained away from the refractory components that freeze into a solid cake (see Section 6.3). To melt a frozen cold cap, charging must be stopped until the cold cap

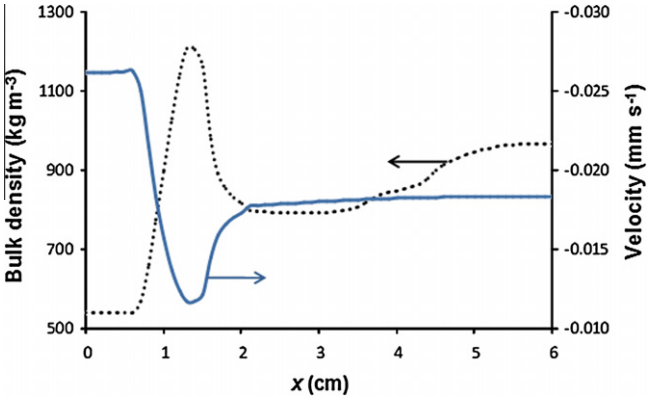

Fig. 7. Bulk density and velocity profiles within cold cap.

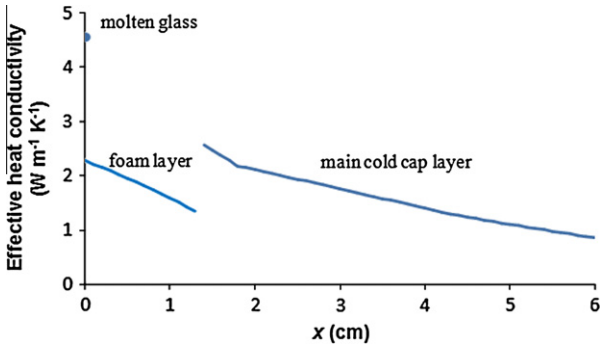

Fig. 9. Effective heat conductivity distribution within cold cap.

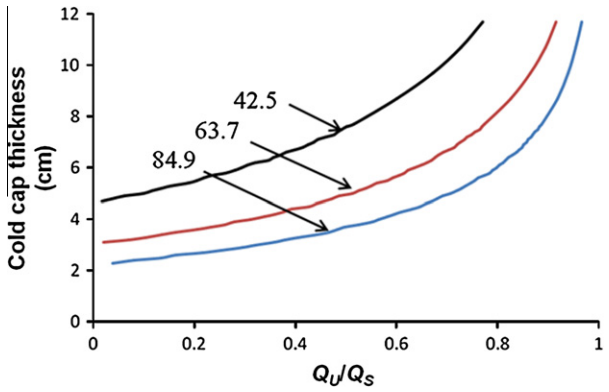

Fig. 10. Cold cap thickness versus upper and total heat flux; numbers represent Q_F in kW m^{-2}.

dissolves in the existing melt, with or without adding fluxes. Melter idling leads to a loss of efficiency.

As Table 2 and Fig. 6 indicate, the heating rate experienced by feed particles within the cold cap varies between 10 and 50 K min^{-1}. According to TGA data, the conversion progress via the mass loss of the melter feed is not substantially affected by the heating rate for heating rates from 1 to 50 K min^{-1}. This justifies our assumption stated at the beginning of this section that the reaction progress could be represented by TGA and DSC data for a constant rate of heating within this interval.

Calculation of the foam layer thickness was based solely on heat transfer. However, the foam thickness is also affected by capillary and pressure forces that are not accounted for in our model. The behavior of foam is discussed in the next section.

5. Foaming

5.1. Rate-controlling steps

For the melting rate controlled jointly by the heat transfer to the cold cap and the reaction kinetics, Hrma [28] obtained the formula:

$$j_M = \frac{j_{MC}^2}{2j_{MH}}\left(\sqrt{1+\frac{4j_{MH}^2}{j_{MC}^2}}-1\right) \tag{31}$$

where

$$j_{MC} = \sqrt{\frac{\lambda_F k\rho(T_M - T_F)}{\Delta H_F}} \tag{32}$$

is the ultimate melting rate achievable by enhancing heat transfer without changing the conversion kinetics and:

$$j_{MH} = \frac{\lambda_M(T_M - T_F)}{\delta_M \Delta H_F} \tag{33}$$

is the heat-transfer-controlled melting rate. In these equations, λ_F represents the effective heat conductivity of the cold cap, k is the conversion rate coefficient, ρ is the feed density, T_F is the feed temperature at the beginning of conversion reactions, ΔH_F is the conversion heat, λ_M is the effective heat conductivity of the melt under the cold cap, T_M is the melter operating temperature, and δ_M is the temperature boundary layer thickness in the melt under the cold cap.

Eqs. (31)–(33) are based on simplifying assumptions:

(1) A dry batch is charged into the melter. Cold cap thickness is controlled by the rate of batch charging, which is uniform over the cold cap surface. Melting heat comes from the molten glass and is consumed in the reaction layer, above which the temperature is uniform.
(2) The heat conductivity and the conversion rate with respect to the conversion enthalpy are constant throughout the reaction layer and the foam layer is not present. Thus, Eqs. (31)–(33) are derived for a model consisting of two layers: the reaction layer in the cold cap and the thermal boundary layer in molten glass.

With this model, the cold cap-bottom temperature and the reaction-layer thickness increase with increasing rate of melting. This is caused by the shift of reactions to higher temperatures when the rate of heating is higher. By Eq. (31), the melting rate will be conversion controlled ($j_M \to j_{MC}$) if the conversion rate is low ($k \to 0$), or the heat transfer rate is high ($\delta_M \to 0$). Under these conditions, the melting rate will be determined by the physical and chemical characteristics of the conversion layer because the conditions in the glass-melt pool will allow the conversion heat to be delivered as needed.

This situation is far from being achieved if a foam layer is present at the bottom of the cold cap. With a foam layer, Eq. (33) can be modified, obtaining:

$$j_{MH} = \frac{(T_M - T_F)}{(\frac{\delta_M}{\lambda_M} + \frac{\delta_f}{\lambda_f})\Delta H_F} \tag{34}$$

where λ_f is the foam-layer effective heat conductivity and Δ_f is the foam-layer thickness.

5.2. Cold cap bottom

Because of boundary conditions, the location of the cold cap bottom is crucial for our model. Three options can be considered:

(1) One option is to identify the cold cap bottom with the boundary between the secondary and the primary foam layers (see Fig. 1) because the former is clearly within the cold cap and the latter is an accumulation of ascending bubbles.
(2) Another option is to identify the cold cap bottom as the point (in 1D representation) at which the foam is no longer sustainable and collapses. This point can be equated with the maximum on the foaming curve, which, as seen in Fig. 4, occurs at ~900 °C in the melter feed under study.
(3) As a third alternative, the bottom is located where the motion of the condensed phase can no longer be considered as one-dimensional and the circular convection of the melt takes over. This probably happens at the bottom of the secondary-foam layer where the temperature is between 1050 and 1150 °C. Thus, secondary foam is not treated as separate from the cold cap.

Options (1) and (2) are recommended for an advanced model in which the foam layers are well defined by mathematical formulation. We have adopted the third option with T_B = 1100 °C as a provisional value for the boundary condition. This seems appropriate for the model of an entire melter in which the cold cap is included. Though the actual T_B depends on δ_M, the value of 1100 °C is deemed realistic for a melter in which forced convection driven by bubbling brings the hot melt in close proximity with the cold cap. The bubbling is introduced by bubblers submerged into the melt.

5.3. Primary foam

Because $\lambda_f \ll \lambda_M$, the temperature difference across the foam layer, $T_B - T_P$, is high. The foam layer insulates the cold cap from the melt and, by Eqs. (31) and (34), becomes a dominant factor for the rate of melting. This makes the rate of conversion less important but, as explained above, a small shift of the reaction-rate peaks influences the rate of melting through its impact on the rate of foaming. Indeed, as Fig. 4 shows, the extent of foaming increases as the heating rate increases. A similar effect was observed for a commercial glass batch by Raether and Kraus [29].

In a high-viscosity melt, such as molten glass, higher gas-phase content means a more insulating, yet relatively stable, foam-layer. Unlike secondary foam, primary foam is not swept away by intense bubbling, and thus affects the rate of melting.

Fig. 4 also shows a shift of the minimum volume by sintering to higher temperatures as a result of an increased heating rate experienced by the feed at a higher rate of melting. However, this shift is not large enough to prevent the increase of foaming caused by an even larger shift of the batch-reaction peaks. Thus, foaming potentially diminishes the effectiveness of performance-augmenting measures, such as increasing the melter-operating temperature, the rate of bubbling, or both.

Primary foam can be decreased, and perhaps entirely eliminated, by an appropriate formulation and preparation of the melter feed. For example, a feed of the same composition as that listed in Table 1, except made with crystalline Al_2O_3 (corundum) instead of $Al(OH)_3$ (gibbsite), melted at an unacceptably slow rate [25] and, as shown in Fig. 11, exhibited ample foaming. Fig. 11 displays the void fraction growth, up to the point of foam collapse, of pellets from melter feeds with three different sources of alumina heated at a constant rate of 5 K min^{-1} [17], demonstrating the large effect of the mineralogical form of alumina on foaming.

5.4. Primary foam movement

As discussed in Section 3.2, pellets expanded to foam that eventually collapsed at ~900–1000 °C. This scenario unfolds similarly within the cold cap except that the melt moves vertically down and bubbles are not capable of ascending fast enough through the viscous melt into the open-porosity zone above.

By the Stokes law, the velocity (v_u) of the gas bubble moving by buoyancy is:

$$v_u = \frac{2}{9}\frac{(\rho_M - \rho_g)}{\mu} g R^2 \tag{35}$$

where ρ_M and ρ_g are the melt and gas densities, respectively, μ is the melt viscosity, and R is the bubble radius. This velocity is superimposed with the velocity of the downward-moving melt.

The average melt velocity through the foam layer is $v_M = j/(\rho_M p)$, where p is the porosity. For $j = 0.0141$ kg m^{-2} s^{-1}, $\rho_M = 2600$ kg m^{-3}, and $p = 0.40$, we get $v_M = 1.03 \times 10^{-5}$ m s^{-1}. By Eq. (35) and since $\rho_g \ll \rho_M$, the critical bubble diameter, $2R_C$, to overcome the velocity of moving melt, i.e., $v_u = v_M$, is $2R_C = (18 v_M \mu/\rho_M g)^{1/2}$. With $\mu = 10^4$ Pa s, this formula yields $2R_C = 8.5$ mm. The open pores close at an even higher viscosity than 10^4 Pa s. Therefore, even a bubble as large as 1 cm in radius is likely to be dragged down to the secondary foam layer region. In melter experiments, bubbles are observed escaping at the periphery of the cold cap and through the vent holes. Only large bubbles created by a bubbler are able to break through the cold cap, creating a vent hole.

This example disregards some important secondary phenomena associated with melt inhomogeneities and dissolving particles of quartz. As has been shown by Schweiger et al. [18], large silica grains tend to form slowly dissolving clusters between which bubbles are freely escaping via passages through melt containing an elevated concentration of boron oxide and possessing a lower viscosity. If the viscosity of the glass-forming melt is as low as 10^2 Pa s, bubbles as small as 1 mm in radius can rise up against the down-moving melt, reach the open-porosity layer, and escape to plenum space. This possibility seems attractive as an option for melt-rate enhancement, but clusters of slowly dissolving quartz that leave behind high-viscosity inhomogeneities are not acceptable because the waste glass may not sufficiently homogenize and would have a low chemical durability.

5.5. Coalescence of foam cells

Under the cold cap, descending primary foam bubbles merge with accumulated secondary foam that can only collapse into larger bubbles and cavities, such as those seen in Figs. 12 and 13. Fig. 12 shows a fragment of the cold cap that formed during the melting of a simulated high-level-waste glass in a laboratory-scale melter and Fig. 13 displays X-ray-tomography images by Choi et al. [30] of melter feeds placed in a platinum beaker heated from below for 22 min. In both examples, foam separates the feed in the cold cap from molten glass. The pockets of gas seen in Fig. 13 can move only sideways to the cold cap edges and the vent holes. Note that this fraction of gas escaping sideways is tiny compared to total evolved gas and thus is neglected in Eqs. (5) and (6).

If most of the foam layer consisted of large flat bubbles or cavities into which both ascending and descending bubbles coalesce, the task of computing the heat transfer rate to the cold cap would greatly simplify. Such cavities would have the form of thin flat layers of gas, similar to those trapped under a solid surface with good wettability (having contact angle $\theta < \pi/2$). According to Iguchi and Ilegbusi [31], thickness of a large flat sessile gas bubble in water under a wettable horizontal surface is ~5 mm. Since the capillary

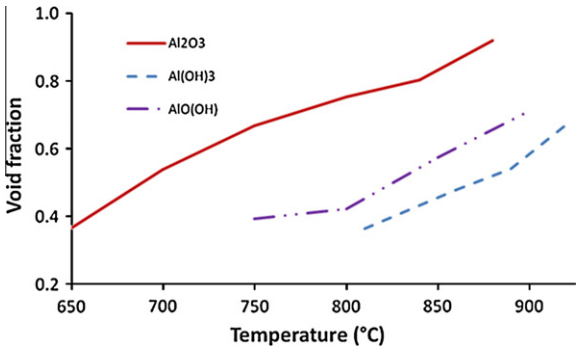

Fig. 11. Void fraction versus temperature of melter feeds with various sources of alumina (5 K min^{-1} heating rate).

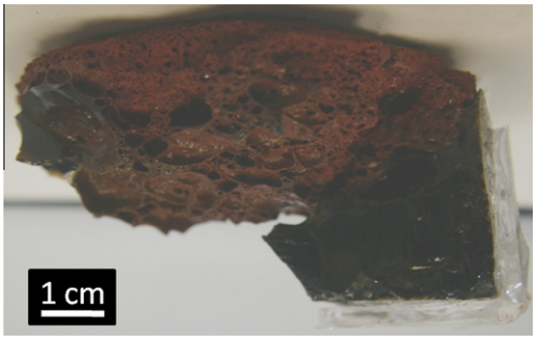

Fig. 12. Cold cap bottom.

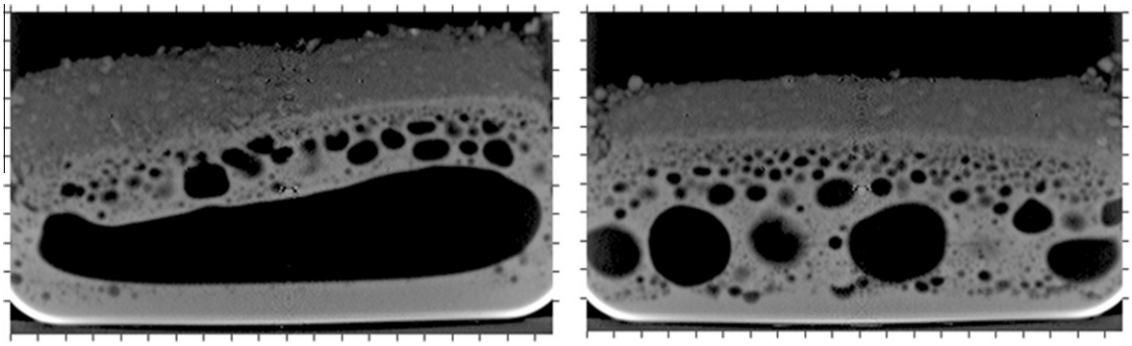

Fig. 13. X-ray tomography images of melter feeds heated from below [30]. The horizontal dimension of the platinum beaker is 10 cm.

thickness is $h_p = 2(\sigma/\rho g)^{1/2}$, where σ is the surface tension, we get for water $h_p \approx 5.5$ mm. For a glass melt with $\sigma \approx 0.275$ N m^{-1} and $\rho \approx 2.6 \times 10^3$ kg m^{-3}, we obtain $h_p \approx 6.6$ mm. Accordingly, the thickness of a large sessile bubble in molten glass can be estimated as ~7 mm.

It is worth mentioning that the foam layer dynamics is not sufficiently understood with respect to its mechanical and thermal properties. Moreover, bubbling introduces large bubbles that probably catch some smaller slowly rising bubbles from redox reactions and sweep foam into vent holes (see Sections 5.2 and 5.3).

The horizontal motion of secondary foam seemingly contradicts the assumption that the circular convection of melt ceases under the foam layer. However, because foam moves as a solid-like body, the cold cap bottom can be identified as the foam–melt interface.

5.6. Heat transfer through foam

Heat transfer through a foam layer or a flat cavity occurs via conduction, convection, and radiation. By Fourier's law, the conductive heat flux can be assessed as $Q_{cond} = \lambda_f(T_2 - T_1)/h_f$, where λ_f is the foam true heat conductivity, T_2 and T_1 are the boundary temperatures, and h_f is the foam layer thickness. With representative values $\lambda_f = 0.08$ W m^{-1} K^{-1}, $T_2 = 1100$ °C, $T_1 = 800$ °C, and $h_f = 6$ mm, $Q_{cond} = 4.0$ kW m^{-2}.

The Rayleigh criterion for the onset of gas convection in a gas bubble or cavity is:

$$\mathrm{Ra} = \frac{g\beta(T_2 - T_1)L^3}{\nu a} \tag{36}$$

where β is the thermal expansion coefficient, ν is the kinematic viscosity, a is the thermal diffusivity of gas inside the bubble and L is the characteristic length (the distance between the colder lower and warmer upper surfaces; in the case of a flat cavity, $L = h_f$). Convection sets in when Ra > 1708 [32]. For typical values $\beta = 0.001$ K^{-1}, $\nu = 138.6 \times 10^{-6}$ m^2 s^{-1}, $a = 3.0 \times 10^{-4}$ m^2 s^{-1}, and $L = 6$ mm, we obtain Ra = 15 < 1708; hence, convection would not arise. The onset of convection would occur at $L \sim 28$ mm. Using the relationship $\mathrm{Nu} = 0.54\,\mathrm{Ra}^{1/4}$ [33], where $\mathrm{Nu} = LQ_{conv}/(\Delta T\lambda)$ is the Nusselt number and $\Delta T = T_2 - T_1$, convection takes place when Nu > 3.5. Then, with $\lambda = 0.08$ W m^{-1} K^{-1}, we get $Q_{conv} > 3.0$ kW m^{-2}. Though the validity of the above relationship has not been established for Ra < 10^4 [33], it seems unlikely that Ra would exceed the critical value in foam bubbles or cavities. Thus, the convective heat transfer through foam appears negligible.

Radiation between two parallel surfaces with known emissivity can be expressed as $Q_{rad} = \sigma(T_2^4 - T_1^4)/(2/\varepsilon - 1)$, where σ is the Stefan–Boltzmann constant ($\sigma = 5.67 \times 10^{-8}$ W m^{-2} K^{-4}), and ε is the emissivity. For molten glass, $\varepsilon = 0.88$, taken from Viskanta and Wu [7]. Thus $Q_{rad} \approx 47$ kW m^{-2}. When compared to the heat transfer by conduction and convection, the radiation heat transfer is dominating.

The heat conductivity of a gas-containing flat cavity can now be estimated as $\lambda_{cav} = h_f(Q_{cond} + Q_{rad})/\Delta T = 1.02$ W m^{-1} K^{-1}. Provided that the fraction of cavities in the foam-layer area equals the maximum void fraction of foam, p, the average $\lambda_f = p\lambda_{cav} + (1 - p)\lambda_M$. Based on 15 K min^{-1}-pellet-expansion data, one obtains $\lambda_f = 1.54$ W m^{-1} K^{-1} ($p = 0.79$ and $\lambda_M \approx 3.5$ W m^{-1} K^{-1}). This value is close to the average λ_f used for calculations (~1.8 W m^{-1} K^{-1}, see Section 4). In a foamy layer with spherical bubbles (plausible structure of primary foam), heat is also conducted and convected by the melt.

Summarizing, thermal radiation is the dominant mode of heat transfer through cellular foam or a cavity and enhances heat transfer through spherical foam or bubbly melt.

Because of uncertainty regarding the structure of the foam layer, the heat transfer through it is difficult to assess, not to mention the effect of melt dragged by incoming bubbles, melt flowing through the foam layer, bubble coalescence, gas escape through vent holes, etc.

6. Discussion

As stated in the Introduction, our ultimate objective is to develop a 3D model of the cold cap (or its axially symmetrical 2D version). In this study, we have developed the simplified 1D model as the first step towards more advanced versions. Limitations of the 1D model are discussed below together with the key factors to be accounted for in the 3D model.

6.1. 1D-model assumptions and melter scaling

The applicability of the 1D model of the cold cap rests upon two assumptions. First, we assume that the model represents the cold cap at every point of the horizontal plane sufficiently distant from the external edges and the vent holes. Second, the 1D model is applicable when all phases and components within the cold cap move in the vertical direction. Only the slurry on the top and the gas cavities and secondary foam at the bottom move horizontally. Consequently, the local cold cap thickness and the melting rate depend only on the boundary heat fluxes that may change with the horizontal coordinates. As a corollary, the average cold cap thickness and melting rate are generally independent of the scale of the melter. This independence has been experimentally confirmed by melter tests conducted under identical or equivalent conditions, such as the intensity of bubbling, melt temperature, or cold cap coverage [25].

6.2. Slurry layer and cold cap spreading

With the fixed upper boundary temperature, the cold cap thickness depends on the heat transfer through its surfaces (Section 4). Because the top surface of the cold cap is covered by slurry, the

upper boundary temperature is ~100 °C. However, this would not be the case if the top surface were dry. Until recently, it had been assumed that a pool of boiling slurry was confined to a small area under the charging nozzle while the rest of the cold cap surface was dry and the cold cap thickness was determined by spreading of the cold cap over the surface of molten glass. Direct observations of the entire cold cap area, which recently became available, show that the slurry is spread over the cold cap surface to the edges. Therefore, we have assumed in this study that it is the slurry that is spreading over the cold cap rather than the cold cap spreading over the melt.

However, observations have yet to confirm this hypothesis for large cold caps in pilot-scale melters. Until then, it is conceivable that a fraction of the surface of a large cold cap can be dry. Since the dry melter feed contains molten salts in the upper layer and glass melt in the lower layer, and rests on a cushion of foam, it can easily spread under gravity and the thickness of the dry portion will then be controlled by cold cap spreading. For this type of spreading, the 1D model would not be representative enough, but a 3D model would be adequate for the task. Such a model would include the balance of momentum and would have to consider the thermorheology of the feed.

6.3. Molten salt mobility and cold-cap freezing

An advanced cold cap model will account for the multiphase nature of the cold cap. The condensed phase consists of two liquids and various solids. The molten salt phase, also called primary melt, is as fluid as water, and thus is highly mobile, whereas the glass-forming phase, also called secondary melt, possesses a high viscosity.

Primary melt easily wets surfaces of solids and molten glass while reacting with them. However, the excess of the primary melt, which is not immobilized by capillary forces in liquid films and bridges, can migrate into porous areas or be drained by gravity [34].

As explained in Section 5.3, high-viscosity glass-forming melt creates a ceiling that primary foam bubbles are unlikely to penetrate. It also creates a bottom barrier that stops primary melt drainage and, because of a higher temperature, gives molten salts a chance to react with the rest of cold cap materials at a faster rate. However, primary melt will also flow horizontally if it has a chance (e.g., at the cold cap edges), leaving behind refractory materials that solidify into a frozen cold cap.

The primary-melt migration is a potentially destabilizing phenomenon that can prevent the steady state from establishing. The task of the advanced model will be to determine the conditions at which the steady state can exist. For cold caps that tend to freeze, the model should determine the optimum periods of melter idling for which serious setbacks can be avoided.

6.4. Horizontal movement of foam and cavities

Gas bubbles accumulate under the cold cap, where they create foam and coalesce into cavities that move sideways to the cold cap edges. Bursting of large bubbles is usually observed in the vent holes and at the melt surface between the steady-state cold cap and walls [35]. Vent holes arise spontaneously or are maintained by bubblers. This phenomenon should be carefully observed and possibly incorporated in the model.

6.5. Other phenomena

Glass-forming melt is initially confined to disconnected pockets that gradually grow and eventually connect into a continuous phase that encapsulates undissolved solids, residues of molten salts, and glass bubbles. Multiple solids, amorphous and crystalline, exist in the cold cap, originating from the melter feed, from batch reactions, and from phase transitions. These solids react with the salt melt and dissolve in the glass melt. They also provide nucleation sites for other phases and gas bubbles. The model should include mass transfer phenomena to represent melt homogenization, melt stirring by bubbles, and dissolution of solid and residual salts, such as sulfates or pertechnetates. These phenomena occur on a micrometer scale. The cold cap model will determine for them the macroscopic conditions in terms of temperature and velocities. If these microscopic phenomena influence macroscopic properties to an extent that cannot be neglected, the advanced model will be modified to account for the coupling.

6.6. Effect of melter feed composition

The structure and the behavior of both primary and secondary foam layers can differ for various types of feeds. Through the appropriate formulation of the feed composition, it may be possible to practically eliminate the primary foam, reduce secondary foam, and, by decreasing viscosity, to accelerate the gas removal.

6.7. Experimental validation

The experimental validation of the cold cap model per se is hardly possible. The purpose of the cold cap model is to predict the rate of melting, but this goal can be achieved only after the cold cap model is incorporated into the overall model of the melter such as that developed by Schill [36]. Only the total model will be capable of determining the heat fluxes, both from below and from above, to the cold cap, and the cold cap bottom temperature. With these coupled boundary conditions, the rate of melting can be correctly determined provided that all other input data are available.

In this work, we proceeded in the reverse order, taking the rate of melting as measured and computed the heat fluxes at the boundaries and the cold cap thickness. Regarding the cold-cap bottom temperature, we used an estimate because precise measurements of this temperature do not exist. In principle, even a 1D model should provide a good service because of the coupling of the temperatures and heat fluxes from molten glass with the rate of melting and cold cap thickness. In fact, the cold cap influences the velocity distribution in the melt to a great extent, e.g., by determining the direction of the melt circulation.

7. Conclusions

The preliminary 1D model for the cold cap in a slurry-fed waste glass melter has been developed. The model solves simplified balances of mass and energy using the finite difference method. The outcome is the temperature and velocity fields within the cold cap.

The rate of melting is determined by the total heat flux to the cold cap that occurs from below (from molten glass) and partly from above (to help evaporate water from the slurry). The response of the cold cap thickness to the boundary heat fluxes can be summarized as follows.

1. If the fraction of the total heat flux to the cold cap that comes from above (to evaporate water from the slurry) is constant, the cold cap thickness decreases as the total heat flux to the cold cap, and thus the rate of melting, increases.
2. At a constant total heat flux (the rate of melting), the cold cap thickness increases as the fraction of heat flux from above increases.

These results are a consequence of defining cold cap boundaries by fixed temperatures (as necessitated by the presence of boiling slurry on the top of the cold cap and foam at its bottom) rather

than by the degree of conversion. While the cold cap thickness decreases with increasing heat flux (and rate of melting), the reaction zone shifts to higher temperatures until the evolution of batch gases overlaps with the development of glass-forming melt, resulting in the appearance of primary foam at the cold cap bottom.

Apart from primary foam, the gas-phase layer under the cold cap also originates from redox reactions in molten glass. Generally, the melt above foam is too viscous and the downward velocity of melt is too high for the gas bubbles to ascend by buoyancy. Gas bubbles and cavities move to the cold cap edges and vent holes where they escape to the plenum space.

As previously suspected but not convincingly argued, yet evidenced from empirical data, the accumulation of the gas phase under the cold cap and its outflow to the free surface of melt limit the heat flux to the cold cap, thus becoming the major controlling factor for the rate of melting. It is recommended that the future advanced cold cap model be 3D, include interactive behavior of the foam layer and the main liquid and solid phases, and be incorporated into the complete model of the melter.

Acknowledgements

The authors are grateful to the U.S. Department of Energy Federal Project Office Engineering Division for the Hanford Tank Waste Treatment and Immobilization Plant for financial support and to Albert Kruger for his assistance and guidance. Richard Pokorny is also pleased to acknowledge support from Czech Grant Agency (GACR No. P106/10/1912). The authors would also like to thank their colleagues at the Pacific Northwest National Laboratory, Dong-Sang Kim and Jaehun Chun, for insightful discussions and David Pierce for providing TGA and DSC data. Pacific Northwest National Laboratory is operated for the U.S. Department of Energy by Battelle under Contract DE-AC05-76RL01830. In its final stages, this research was supported by WCU (World Class University) program through the National Research Foundation of Korea funded by the Ministry of Education, Science and Technology (R31 - 30005).

References

[1] W.S. Kuhn, Mathematical modeling of batch melting in glass tanks, in: D. Krause, H. Loch (Eds.), Mathematical Simulation in Glass Technology, Springer, 2002.
[2] C. Moukarzel, W.S. Kuhn, Glass Sci. Technol. 76 (2003) 81–90.
[3] Z. Feng, D. Li, G. Qin, S. Liu, J. Am. Ceram. Soc. 91 (2008) 3229–3234.
[4] A. Abbassi, Kh. Khoshmanesh, Appl. Therm. Eng. 28 (2008) 450–459.
[5] C.C. Yen, W.S. Hwang, Mater. Trans. 49 (2008) 766–773.
[6] H. Mase, K. Oda, J. Non-Cryst. Solids 38–39 (1980) 807–812.
[7] R. Viskanta, X. Wu, J. Am. Ceram. Soc. 67 (1984) 376–380.
[8] A. Ungan, R. Viskanta, AIChE Sym. Ser. 80 (236) (1984) 446–451.
[9] P. Hrma, Glastech. Ber. 55 (1982) 138–150.
[10] P. Schill, Ceram.-Silik. 26 (1982) 155–163. in Czech.
[11] P. Schill, Ceram.-Silik. 26 (1982) 209–222. in Czech.
[12] R. Pokorny, P. Hrma, Mathematical Model of Cold Cap – Preliminary One-Dimensional Model Development, PNNL-20278, Pacific Northwest National Laboratory, Richland, Washington, 2011.
[13] P. Hrma, A.A. Kruger, R. Pokorny, J. Non-Cryst. Solids (2012), http://dx.doi.org/10.1016/j.jnoncrysol.2012.01.051.
[14] P. Schill, J. Chmelar, J. Non-Cryst. Solids 345&346 (2004) 771–776.
[15] P. Hrma, M.J. Schweiger, C.J. Humrickhouse, J.A. Moody, R.M. Tate, T.T. Rainsdon, N.E. TeGrotenhuis, B.M. Arrigoni, J. Marcial, C.P. Rodriguez, B.H. Tincher, Ceram.-Silik. 54 (2010) 193–211.
[16] S.H. Henager, P. Hrma, K.J. Swearingen, M.J. Schweiger, J. Marcial, N.E. TeGrotenhuis, J. Non-Cryst. Solids 357 (2011) 829–835.
[17] D.A. Pierce, P. Hrma, J. Marcial, B.J. Riley, M.J. Schweiger, Int. J. Appl. Glass Sci. 3 (2012) 59–68.
[18] M.J. Schweiger, P. Hrma, C.J. Humrickhouse, J. Marcial, B.J. Riley, N.E. TeGrotenhuis, J. Non-Cryst. Solids 356 (2010) 1359–1367.
[19] R. Pokorny, D.A. Pierce, P. Hrma, Thermochim. Acta 541 (2012) 8–14.
[20] S.A. Lottes, M. Petrick, Glass Furnace Model (GFM) Development and Technology Transfer Program Final Report, ANL-07/28, Argonne National Laboratory, Argonne, Illinois, 2007.
[21] A.J. Faber, R.G.C. Beerkens, H. de Waal, Glastech. Ber. 65 (1992) 177–185.
[22] R. Conradt, P. Suwannathada, P. Pimkhaokham, Glastech. Ber. 67 (1994) 103–113.
[23] N.S. Kham, Development of Methods for the Characterization of Melting Batches, Thesis, Rheinisch-Westfälichen Technischen Hochschule, Aachen, Germany, 2005.
[24] P. Schill, Modeling the behavior of noble metals during HLW vitrification, in: W. Lutze, Modeling the behavior of noble metals during HLW vitrification in the DM1200 melter, VSL-05R5740-1, Vitreous State Laboratory, Washington DC, 2005.
[25] K.S. Matlack, H. Gan, M. Chaudhuri, W. Kot, W. Gong, T. Bardakci, I.L. Pegg, J. Innocent, DM100 and DM1200 Melter Testing with High Waste Loading Glass Formulations for Hanford High-aluminum HLW Streams, VSL-10R1690-1, Vitreous State Laboratory, The Catholic University of America, Washington, DC, 2010.
[26] P.A. Smith, J.D. Vienna, P. Hrma, J. Mater. Res. 10 (1995) 2137–2149.
[27] J.G. Darab, E.M. Meiers, P.A. Smith, Mat. Res. Soc. Proc. 556 (1999) 215–222.
[28] P. Hrma, Glastech. Ber. 63K (1990) 360–369.
[29] F. Raether, M. Krauss, Glass Sci. Technol. 77 (2004) 118–123.
[30] A.S. Choi, D.H. Miller, D.M. Immel, Determination of HLW glass melt rate using X-ray computed tomography (CT), SRNL-STI-2010-00767, Rev. 0, Savannah River National Laboratory, Aiken, South Carolina, 2010.
[31] M. Iguchi, J.O. Ilegbusi, Modeling Multiphase Materials Processes: Gas-liquid Systems, Springer, New York, 2010.
[32] D.A. Nield, J. Fluid Mech. 81 (1977) 513–522.
[33] F.P. Incropera, D.P. DeWitt, Fundamentals of Heat and Mass Transfer, fourth ed., Wiley, 1996.
[34] P. Hrma, L.M. Bagaasen, M.J. Schweiger, M.B. Evans, B.T. Smith, B.M. Arrigoni, D.-S. Kim, C.P. Rodriguez, S.T. Yokuda, J. Matyas, W.C. Buchmiller, A.B. Gallegos, A. Fluegel, Bulk Vitrification Performance Enhancement: Refractory Lining Protection Against Molten Salt Penetration, PNNL-16773, Pacific Northwest National Laboratory, Richland, Washington, 2007.
[35] D.S. Kim, M.J. Schweiger, W.C. Buchmiller, J. Matyas, Laboratory-Scale Melter for Determination of Melting Rate of Waste Glass Feeds, PNNL-21005; EMSP-RPT-012, Pacific Northwest National Laboratory, Richland, Washington, 2012.
[36] P. Schill, W. Lutze, W. Gong, I.L. Pegg, Glass Technol.-Part A 48 (2007) 276–289.